HOKKAIDO UNIVERSITY

Title	A Numerical Study of Convection in a Condensing CO2 Atmosphere under Early Mars-Like Conditions
Author(s)	Yamashita, Tatsuya; Odaka, Masatsugu; Sugiyama, Ko-Ichiro et al.
Citation	Journal of the atmospheric sciences, 73(10), 4151-4169 https://doi.org/10.1175/JAS-D-15-0132.1
Issue Date	2016-10
Doc URL	https://hdl.handle.net/2115/64937
Rights	© Copyright [2016.10] American Meteorological Society (AMS). Permission to use figures, tables, and brief excerpts from this work in scientific and educational works is hereby granted provided that the source is acknowledged. Any use of material in this work that is determined to be "fair use" under Section 107 of the U.S. Copyright Act September 2010 Page 2 or that satisfies the conditions specified in Section 108 of the U.S. Copyright Act (17 USC §108, as revised by P.L. 94-553) does not require the AMS's permission. Republication, systematic reproduction, posting in electronic form, such as on a web site or in a searchable database, or other uses of this material, except as exempted by the above statement, requires written permission or a license from the AMS. Additional details are provided in the AMS Copyright Policy, available on the AMS Web site located at (https://www.ametsoc.org/) or from the AMS at 617-227-2425 or copyrights@ametsoc.org.
Type	journal article
File Information	JAS-D-15-0132.1.pdf

Hokkaido University Collection of Scholarly and Academic Papers : HUSCAP

A Numerical Study of Convection in a Condensing CO_2 Atmosphere under Early Mars-Like Conditions

TATSUYA YAMASHITA,[a] MASATSUGU ODAKA,[b] KO-ICHIRO SUGIYAMA,[c,g] KENSUKE NAKAJIMA,[d] MASAKI ISHIWATARI,[b] SEIYA NISHIZAWA,[e] YOSHIYUKI O. TAKAHASHI,[f] AND YOSHI-YUKI HAYASHI[f]

[a] *Geodetic Department, Geospatial Information Authority of Japan, Tsukuba, Japan*
[b] *Department of Cosmosciences, Hokkaido University, Sapporo, Japan*
[c] *Institute of Space and Astronautical Science, Sagamihara, Japan*
[d] *Department of Earth and Planetary Sciences, Kyushu University, Fukuoka, Japan*
[e] *RIKEN Advanced Institute for Computational Science, Kobe, Japan*
[f] *Department of Planetology, and Center for Planetary Science, Kobe University, Kobe, Japan*

(Manuscript received 7 May 2015, in final form 27 January 2016)

ABSTRACT

Cloud convection of a CO_2 atmosphere where the major constituent condenses is numerically investigated under a setup idealizing a possible warm atmosphere of early Mars, utilizing a two-dimensional cloud-resolving model forced by a fixed cooling profile as a substitute for a radiative process. The authors compare two cases with different critical saturation ratios as condensation criteria and also examine sensitivity to number mixing ratio of condensed particles given externally.

When supersaturation is not necessary for condensation, the entire horizontal domain above the condensation level is continuously covered by clouds irrespective of number mixing ratio of condensed particles. Horizontal-mean cloud mass density decreases exponentially with height. The circulations below and above the condensation level are dominated by dry cellular convection and buoyancy waves, respectively.

When 1.35 is adopted as the critical saturation ratio, clouds appear exclusively as intense, short-lived, quasi-periodic events. Clouds start just above the condensation level and develop upward, but intense updrafts exist only around the cloud top; they do not extend to the bottom of the condensation layer. The cloud layer is rapidly warmed by latent heat during the cloud events, and then the layer is slowly cooled by the specified thermal forcing, and supersaturation gradually develops leading to the next cloud event. The periodic appearance of cloud events does not occur when number mixing ratio of condensed particles is large.

1. Introduction

In the Martian atmosphere, the major constituent, CO_2, condenses, in contrast to Earth's atmosphere where a minor constituent, H_2O, does. Investigation of possible structures of circulation fields and properties of clouds in such an atmosphere, especially a dense CO_2 atmosphere, is not only interesting as a problem of fluid mechanics, but also as an important target of research on the early Mars, where the scattering greenhouse effect of CO_2 ice cloud could have played an indispensable role in maintaining possible warm climate (Forget and Pierrehumbert 1997; Mischna et al. 2000; Colaprete and Toon 2003; Mitsuda 2007; Forget et al. 2013). Previous studies have shown that the intensity of scattering greenhouse effect depends on a number of cloud properties, such as the size distribution of cloud particles, optical depth, cloud cover, and cloud height (Forget and Pierrehumbert 1997; Mischna et al. 2000; Kitzmann et al. 2013). For the advancement of our understanding on the early Martian

Denotes Open Access content.

[g] Current affiliation: Department of Information Engineering, National Institute of Technology, Matsue College, Matsue, Japan.

Corresponding author address: Masatsugu Odaka, Department of Cosmosciences, Graduate School of Science, Hokkaido University, Science Bldg. 8-202, Kita-10, Nishi-8, Kita-Ku, Sapporo 060-0810, Japan.
E-mail: odakker@gfd-dennou.org

DOI: 10.1175/JAS-D-15-0132.1

© 2016 American Meteorological Society

Publisher's Note: This article was revised on 7 October 2016 to correct a typographical error in the third author's name.

climate, it is, therefore, valuable to investigate possible properties of CO_2 clouds consistent with circulation fields of convection associated with condensation of the major atmospheric constituent.

There has been almost no literature considering convection with condensation of the major constituent of the atmosphere by explicitly solving convective motion. In the previous studies employing one-dimensional models, distributions of cloud particles are specified irrelevant to flow fields. Forget and Pierrehumbert (1997) and Mischna et al. (2000), for instance, assume that clouds are localized at specified vertical levels in the condensation layer. Mitsuda (2007) determines the equilibrium distribution of cloud condensates by the local radiative balance, neglecting possible contributions of atmospheric motion and latent heating. The model employed by Colaprete and Toon (2003) includes detailed microphysical schemes considering aerosol and CO_2 cloud particles with a representation of the particle size distribution, but is a vertical one-dimensional model that is incapable of resolving convective flow explicitly, although a parameterized eddy diffusion scheme is included to account the convective transfers.

In studies employing atmospheric general circulation models (GCMs), the details of those unknown processes of condensation and convection of a thick CO_2 atmosphere have been modeled only crudely or simply substituted with those for the parameterization schemes developed for Earth's and/or the present Martian atmospheres whose validity in early Martian condition is unclear. Sabato (2008) employs the moist convective adjustment scheme to realize GCM calculations of a thick CO_2 atmosphere of early Mars for the purpose of investigating possible behaviors of baroclinic waves there. In their GCM, condensates are immediately removed, and clouds are assumed to exist in the updraft regions above the condensation level. Forget et al. (2013) employs, in addition to the convective adjustment, a large-scale condensation scheme where particle size is diagnosed by the amount of condensate and specified, fixed number of condensation nuclei, and argues that CO_2 ice clouds of early Mars exist in a wide latitudinal range from the tropics to the pole with thick vertical extent from the condensation level to the tropopause. In the GCM calculation of present-day Martian atmosphere by Colaprete et al. (2008), a more detailed microphysical scheme is included, where particle size spectrum and its temporal evolution are diagnosed by two moment scheme. However, the convective mixing scheme incorporated in the model (whose conceptual framework is illustrated in Fig. 11 of the paper) is constructed assuming a particular behavior of convective motion in mind, whose validity in the possible dense early Martian atmosphere is unclear, although one could accept it as validated in the present-day atmosphere based on the overall performance of GCM as a whole. Although a more sophisticated cloud parameterization scheme should be implemented to proceed with further arguments, we are not guaranteed to model the effects of convection following the experiences obtained from Earth's atmosphere, since the features of convection associated with condensation of the major atmospheric constituent may be completely different from those of cloud convection of Earth's atmosphere.

A peculiar aspect of thermal convection with condensation of the major atmospheric constituent is that a quasi-equilibrium condensing air parcel can hardly be positively buoyant, since temperature of the condensing air parcel is constrained by the saturation vapor pressure curve and should be the same as that of the environment of the same pressure level. This is a feature quite different from that of the moist convection of Earth's atmosphere, where condensates are the minor component. As far as the authors know, the only study that investigates the features of condensing convection of CO_2 atmosphere is Colaprete et al. (2003), where a vertical one-dimensional entraining plume model is employed to study CO_2 ice clouds in the polar nights of the present Martian atmosphere. They argue that, if supercooling is not permitted in the environment, a condensing air parcel cannot obtain buoyancy, while if supercooling is permitted as is often observed in Martian polar night regions, a condensing air parcel can obtain buoyancy and its vertical ascent can be sustained to produce a CO_2 ice cloud. However, since the model they utilized is a simple plume model, it is beyond the scope of their study to investigate circulation features of condensing convection, associated cloud distributions, and "climatological"-mean temperature profiles of the environment, which ought to be realized through a large number of convective cycles.

We conduct here a qualitative investigation on the characteristics of circulation fields and distributions of clouds that develop in convection associated with condensation of the major component, CO_2, under a condition idealizing possible tropical region of early Mars. More specifically, we focus on the structure of condensing CO_2 atmospheric convection driven by a spatially uniform, temporally constant body cooling over a flat homogeneous surface of constant temperature without any large-scale dynamical forcing. For simplicity, any complex feedbacks, such as cloud radiation interaction, are excluded. The idea is that investigation of possible characteristics of condensing convection realized under such a GFD setup should provide useful knowledge to proceed for examining condensing convection under more realistic conditions affected by active radiative processes such as diurnal variation, surface topography, large-scale disturbances, or other complex feedbacks.

For this purpose, we perform a series of long-term numerical simulations of convection, explicitly considering physics of CO_2 ice clouds and dynamics of convective circulations, until statistical equilibrium states are reached. Our motivation in pursuing statistical equilibrium states is to examine convective motion and cloud distribution in the environment that is spontaneously established through statistical contributions of a large number of clouds over multiple life cycles rather than to investigate formation and dissipation of a single cloud in a specified environment. This is a strategy following, for instance, Held et al. (1993), Tompkins (2001), and Wing and Emanuel (2014) for Earth's atmosphere and Sugiyama et al. (2011, 2014) for the Jovian atmosphere. The numerical model we use is a cloud-resolving model that we have been developing for investigating a variety of atmospheric convection from the viewpoint mentioned above, and to which, for the present study, we have implemented CO_2 ice cloud physics that allows supersaturation. We choose a horizontal and vertical two-dimensional system that demands less computational resources to realize long-term simulations required to reach statistically steady states. In order to improve our understanding step by step, we employ a simplified CO_2 cloud physics similar to that of Tobie et al. (2003) and consider only condensation–evaporation and gravitational sedimentation, neglecting coalescence and breakup of particles.

We focus on dependence of the properties of convective motion and cloud distribution on the values of the critical saturation ratio, the ratio of pressure at the onset of condensation to saturation vapor pressure, and number mixing ratio of condensed particles. The value of critical saturation ratio is expected to affect the degree of supercooling in the resulting atmosphere and, therefore, greatly modify the properties of convective motion and cloud distribution. In this study, we adopt 1 and 1.35 as the values of critical saturation ratio. Number mixing ratio of condensed particles is not only poorly constrained but also varies as a result of dynamics within the model. Here, for the sake of simplicity, we assume it to be temporally constant and spatially uniform; three widely different values are used to explore the sensitivity.

The details of the cloud-resolving model utilized here are described in section 2, and the setup of the experiment, including the choice of the values of critical saturation ratio and number mixing ratio of condensed particles, is described in section 3. In section 4, the results of the experiment are presented mainly focusing on the features of flow fields and cloud distributions in the statistically equilibrium states. Sensitivity of those features to number mixing ratio of condensed particles is presented in section 5. Quantitative aspects of the results are discussed in section 6, and concluding remarks are presented in section 7.

2. Description of cloud-resolving model

The model we utilize is the nonhydrostatic model "deepconv" of GFD Dennou Club (e.g., Sugiyama et al. 2009, 2011, 2014), available at http://www.gfd-dennou.org/library/deepconv/, supplemented with CO_2 cloud microphysics.

a. Formulation

We assume that the atmosphere is an ideal gas and consists entirely of CO_2. The governing equations are two-dimensional quasi-compressible equations with condensation of CO_2. All CO_2 cloud particles are assumed to be solid and fall with terminal velocity depending on the size of cloud particle, as given later.

The equations of motion, the pressure equation, the thermodynamic equation, and the mass equation for CO_2 ice can be written as

$$\frac{du}{dt} = -c_p\bar{\theta}\frac{\partial\Pi'}{\partial x} + D_m(u), \tag{1}$$

$$\frac{dw}{dt} = -c_p\bar{\theta}\frac{\partial\Pi'}{\partial z} + g\frac{\theta'}{\bar{\theta}} - g\frac{R}{p_0}\frac{\bar{\theta}}{\bar{\Pi}^{c_v/R}}\rho_s + D_m(w), \tag{2}$$

$$\frac{\partial\Pi'}{\partial t} + \frac{\overline{c^2}}{c_p\bar{\rho}\bar{\theta}^2}\left[\frac{\partial(\bar{\rho}\bar{\theta}u)}{\partial x} + \frac{\partial(\bar{\rho}\bar{\theta}w)}{\partial z}\right] = \frac{\overline{c^2}}{c_p\bar{\rho}\bar{\theta}}\left(\frac{L}{c_p\bar{\theta}\bar{\Pi}} - 1\right)M_{\mathrm{cond}} + \frac{\overline{c^2}}{c_p\bar{\theta}^2\bar{\Pi}}(Q_{\mathrm{dis}} + Q_{\mathrm{rad}}), \tag{3}$$

$$\frac{d\theta'}{dt} + w\frac{\partial\bar{\theta}}{\partial z} = \frac{1}{\bar{\Pi}}\left(\frac{LM_{\mathrm{cond}}}{\bar{\rho}c_p} + Q_{\mathrm{dis}} + Q_{\mathrm{rad}}\right) + D_h(\theta'), \tag{4}$$

and

$$\frac{\partial\rho_s}{\partial t} + \frac{\partial(\rho_s u)}{\partial x} + \frac{\partial(\rho_s w)}{\partial z} = M_{\mathrm{cond}} + M_{\mathrm{fall}} + D_h(\rho_s), \tag{5}$$

where

$$\frac{d}{dt} = \frac{\partial}{dt} + u\frac{\partial}{\partial x} + w\frac{\partial}{\partial z}, \tag{6}$$

$$D_m(\cdot) = \frac{\partial}{\partial x}\left[K_m\frac{\partial(\cdot)}{\partial x}\right] + \frac{1}{\bar{\rho}}\frac{\partial}{\partial z}\left[\bar{\rho}K_m\frac{\partial(\cdot)}{\partial z}\right], \quad \text{and} \tag{7}$$

$$D_h(\cdot) = \frac{\partial}{\partial x}\left[K_h\frac{\partial(\cdot)}{\partial x}\right] + \frac{1}{\bar{\rho}}\frac{\partial}{\partial z}\left[\bar{\rho}K_h\frac{\partial(\cdot)}{\partial z}\right], \tag{8}$$

where x and z are horizontal and vertical coordinates, respectively, t is time, u and w are horizontal and vertical components of velocity, the overbar ($^-$) denotes the basic state that depends only on height, the prime ($'$)

denotes the perturbation from the basic state, the dot in $(\cdot)$ stands for a variable, ρ is density of CO_2 gas, ρ_s is density of CO_2 ice cloud, and Π and θ are Exner function and potential temperature, which are defined as

$$\Pi = \left(\frac{p}{p_0}\right)^{R/c_p}, \quad \theta = \frac{T}{\Pi}, \tag{9}$$

where T and p are temperature and pressure, respectively. We specify the value of p_0, the reference pressure, to 2.0×10^5 Pa, which is the initial surface pressure. The profiles of the physical quantities of the basic state will be described in section 3. The quantity $\overline{c}$ is the sound velocity given by basic-state temperature as

$$\overline{c}^2 = \frac{c_p}{c_v} R\overline{\theta}\,\overline{\Pi}. \tag{10}$$

The coefficients K_m and K_h are the turbulent diffusion coefficients for momentum and scalar, $Q_{\rm dis}$ and $Q_{\rm rad}$ are the dissipative heating term and the radiative forcing term, and $M_{\rm cond}$ and $M_{\rm fall}$ are the tendency terms of cloud density due to condensation and/or evaporation of CO_2 and gravitational sedimentation of CO_2 ice, respectively. The effect of consumption of gas phase associated with condensation is considered in Eq. (3).

The values of K_m, K_h, and $Q_{\rm dis}$ are calculated by using the 1.5th-order closure scheme of Klemp and Wilhelmson (1978). The surface fluxes of momentum and heat are calculated using the bulk formula of Louis (1979). For simplicity, we fix the value of the coefficient C_* in Eq. (20) of Louis (1979) to 7.4 for both momentum and heat. The profile of $Q_{\rm rad}$, which we adopt as a substitute of radiative processes, depends only on height and will be specified in section 3. The quantity $L = 5.86 \times 10^5\,{\rm J\,kg^{-1}}$ is latent heat of fusion; $c_p = 860.0\,{\rm J\,K^{-1}\,kg^{-1}}$ and $c_v = 671.1\,{\rm J\,K^{-1}\,kg^{-1}}$ are specific heat for constant pressure and constant volume, respectively; $R = 188.9\,{\rm J\,K^{-1}\,kg^{-1}}$ is CO_2 gas constant per mass; and $g = 3.72\,{\rm m\,s^{-2}}$ is the acceleration of gravity.

b. Cloud microphysics

We assume that cloud particles are spherical and form on spherical condensation nuclei and the size of cloud particles is uniform in each grid box. We also assume that number mixing ratio of condensed particles N_* is homogeneous in space and time, whose values we adopt for our experiments will be described in section 3. Radius of each cloud particle r_c can then be related to ρ_s as

$$r_c = \left(r_{\rm as}^3 + \frac{3\rho_s}{4\rho_I \pi \overline{\rho} N_*}\right)^{1/3}, \tag{11}$$

where $\rho_I = 1.565 \times 10^3\,{\rm kg\,m^{-3}}$ is density of CO_2 ice and $r_{\rm as}$ is the radius of condensation nuclei, which is fixed to be 1.0×10^{-7} m, the value mentioned in Tobie et al. (2003) as the lower limit of size of aerosols operating as nuclei. Results are insensitive to the choice of the value of $r_{\rm as}$ as long as it is larger than the present one (not shown here).

The quantity $M_{\rm cond}$, whose amount is given also based on Tobie et al. (2003), is given by

$$M_{\rm cond} = f_{\rm SW} \times \frac{4\pi r_c \overline{\rho} N_* k R \theta^2 \Pi^2}{L^2}(S-1), \tag{12}$$

where $f_{\rm SW}$ is a switch parameter explained below in Eq. (14) whose value is 1 or 0, and $k = 4.8 \times 10^{-3}\,{\rm W\,m^{-1}\,K^{-1}}$ is the thermal diffusion coefficient of CO_2 gas. And,

$$S \equiv \frac{p}{p_*(T)}$$

is saturation ratio of CO_2, where p is pressure and $p_*(T)$ is saturation vapor pressure of CO_2, which we calculate here using a simplified Antoine equation (The Society of Chemical Engineers Japan 1999),

$$p_*(T) = A_{\rm ant} \exp\left(-\frac{B_{\rm ant}}{T}\right), \tag{13}$$

where $A_{\rm ant} = 7.94 \times 10^{11}$ Pa and $B_{\rm ant} = 3103.0$ K. It is noted that we have omitted Kelvin correction in Eq. (12). Considering the short time scale of particle growth ($\sim 10^{-1}$ s) in typical size range (Colaprete and Toon 2003), this simplification is effectively equivalent to using a slightly smaller value of $S_{\rm cr}$ by the amount corresponding to Kelvin correction, which is about 0.04 for the value of $r_{\rm as}$ employed in this study.

We assume that, in the presence of cloud particles, condensation occurs if $S \geq 1$ and evaporation occurs if $S < 1$. On the other hand, in the absence of cloud particles, we assume condensation occurs only if S is larger than the critical saturation ratio, $S_{\rm cr}$, whose value is specified as an experimental parameter and is described in section 3. In the actual numerical calculations, presence of cloud particles for the judgment of condensation is declared when $\rho_s \geq \rho_s^T$, where ρ_s^T is a small positive threshold cloud density. The conditions above are implemented as specifying the switch parameter $f_{\rm SW}$, in Eq. (12) as

$$f_{\rm SW} = \begin{cases} 1 & (\rho_s \geq \rho_s^T \quad \text{and/or} \quad S \geq S_{\rm cr}) \\ 0 & (\rho_s < \rho_s^T \quad \text{and} \quad S < S_{\rm cr}) \end{cases}, \tag{14}$$

where ρ_s^T is introduced to inhibit unphysical expansion of condensation region in the model caused by the discretization error. If the value of ρ_s^T is zero or too small, once condensation occurs on a grid point in a supersaturated area, occurrence of condensation expands quickly around

the point at a physically unreasonable rate depending on the values of time step and grid spacing. In this study, we adopt the value of ρ_s^T to be $1.0 \times 10^{-6}\,\mathrm{kg\,m^{-3}}$ based on trial and error.

The quantity M_{fall} is given by

$$M_{\mathrm{fall}} = \frac{\partial}{\partial z}(\rho_s V_{\mathrm{term}}), \tag{15}$$

where V_{term} is the terminal velocity of cloud particles, which is calculated by using Stokes's law with the Cunningham correction (Forget et al. 2013) as

$$V_{\mathrm{term}} = C_{\mathrm{sc}} \frac{2 r_c^2 g \rho_I}{9\eta}, \tag{16}$$

where η is viscosity coefficient of CO_2 gas, which is calculated by using Sutherland's formula as

$$\eta = \eta_{\mathrm{ref}} \left(\frac{T_{\mathrm{ref}} + C_{\mathrm{CO_2}}}{\overline{\theta}\,\overline{\Pi} + C_{\mathrm{CO_2}}} \right) \left(\frac{\overline{\theta}\,\overline{\Pi}}{T_{\mathrm{ref}}} \right)^{3/2}, \tag{17}$$

where $\eta_{\mathrm{ref}} = 1.47 \times 10^{-5}\,\mathrm{Pa\,s}$ and $T_{\mathrm{ref}} = 293\,\mathrm{K}$ are the reference values of viscosity coefficient and temperature, respectively, and $C_{\mathrm{CO_2}} = 240\,\mathrm{K}$ is Sutherland constant for CO_2 gas (Kaye and Laby 1995). The coefficient C_{sc} is the Cunningham correction factor, which, following Rossow (1978) and Tobie et al. (2003), we calculate as

$$C_{\mathrm{sc}} = 1 + \frac{4}{3} K_n, \tag{18}$$

where $K_n = \lambda / r_c$ is Knudsen number for a cloud particle and λ is the mean free path for the CO_2 molecule, which is calculated from the relation (Chapman and Cowling 1970)

$$\lambda = \frac{k_B \overline{\theta}}{\sqrt{2}\pi\sigma^2 p_0 \overline{\Pi}^{c_v/R}}, \tag{19}$$

where $\sigma = 3.3 \times 10^{-10}\,\mathrm{m}$ is the effective diameter of CO_2 molecules (Golden and Sircar 1994) and $k_B = 1.38 \times 10^{-23}\,\mathrm{m^2\,kg\,s^{-2}\,K^{-1}}$ is Boltzmann constant.

c. *Discretization*

We employ Arakawa-C grid (Arakawa and Lamb 1977) for horizontal direction and Lorenz grid (Lorenz 1960) for vertical direction. The spatial derivatives are evaluated by using a fourth-order centered difference scheme for advection terms and second-order centered difference scheme for the other terms. We employ the time-splitting method of Klemp and Wilhelmson (1978) for time discretization; the sound wave terms and the condensation terms are integrated with a short time step by using a horizontally explicit–vertically implicit scheme, and the other terms are integrated with a long time step by using the leapfrog scheme with Asselin time filter (Asselin 1972).

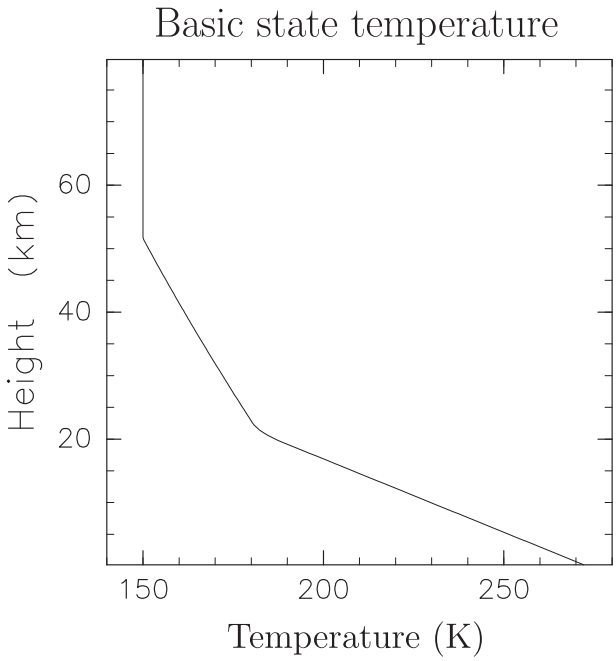

FIG. 1. Temperature profile of the basic state.

3. Experimental setup

The computational domain size is 100 km in the horizontal direction and 80 km in the vertical direction. The grid spacings in the horizontal and vertical directions are 500 and 400 m, respectively. As the basic state, we assume that the atmosphere is cloud free, motionless, and in hydrostatic equilibrium. We specify temperature in the basic state consulting Kasting (1991), assuming that early Mars was warm. Specifically, we set pressure and temperature at the bottom of the atmosphere to be 2.0×10^5 Pa and 273 K, respectively. The vertical temperature profile follows the dry adiabatic profile below the altitude of 20-km height, the saturation temperature profile from 20 to 50 km, and isotherm of 150 K above 50 km (Fig. 1). Initial field is set to be the same as the basic field, except for the random potential temperature disturbances whose maximum amplitude is 1 K introduced at the lowest level to seed convective motion. We fix the temperature of the ground surface to a horizontally uniform and temporally constant value of 273 K. We set the cooling Q_{rad} in Eq. (4) to be $-0.1\,\mathrm{K\,day^{-1}}$ from the bottom of the atmosphere to the altitude of 50 km, consulting a reproduction of the radiative–convective equilibrium calculations under early Mars condition of Kasting (1991) by Mitsuda (2007). We introduce a Newtonian cooling and a

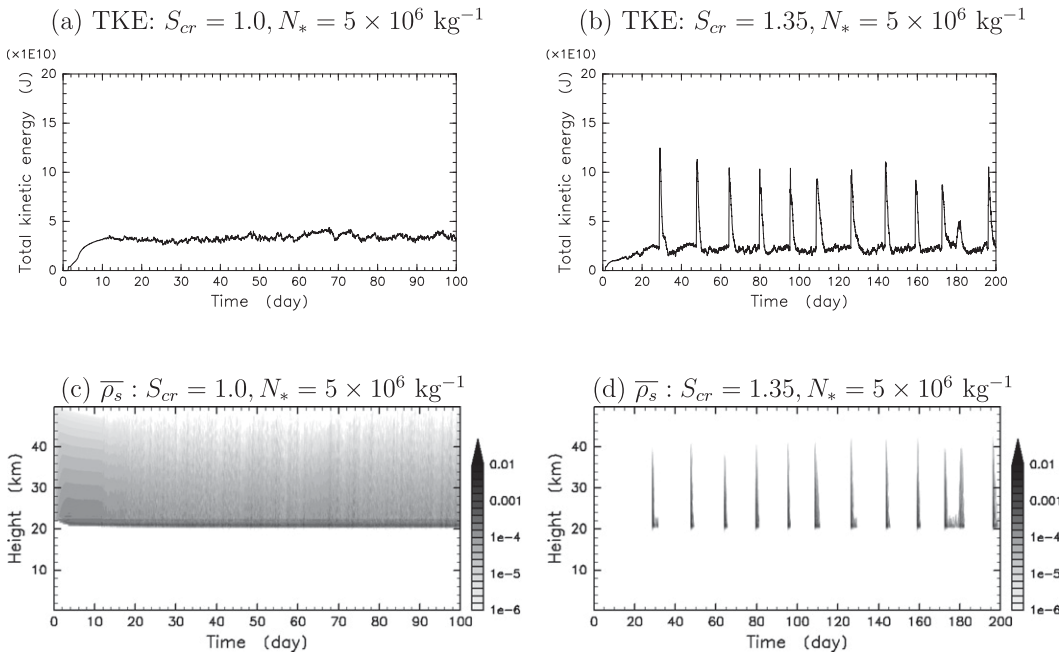

FIG. 2. Temporal evolutions of (a),(b) total kinetic energy (J × 10^{10}) and (c),(d) horizontal-mean cloud density (kg m^{-3}) for the two runs using two different values of S_{cr} with $N_* = 5.0 \times 10^6$ kg^{-1}. (a),(c) The evolutions from 0 to 100 days are shown for the case with $S_{cr} = 1.0$ and (b),(d) the evolutions from 0 to 200 days are shown for the case with $S_{cr} = 1.35$. In (c) and (d), a logarithmic gray scaling is used with minimum value of shading set as $\rho_s = \rho_s^T = 10^{-6}$ kg m^{-3}.

Rayleigh friction above 50-km height, whose time constants are both 3.0×10^4 s, to prevent internal gravity waves reflected from the upper boundary from affecting the region under main consideration.

As for the value of the critical saturation ratio S_{cr}, we adopt two values: 1.0 and 1.35. The latter value is derived by Glandorf et al. (2002) through laboratory experiments. Although their experiments are conducted under the present Martian condition, this value has often been employed also in numerical simulations for the early Mars condition (e.g., Colaprete and Toon 2003; Forget et al. 2013). Number mixing ratio of condensed particles N_* depends not only on abundance of aerosols operating as condensation nuclei but, presumably, also on the properties of convective motion such as induced rate of cooling of parcels; for example, Colaprete and Toon (2003) shows that, because a small number of initial particles grow rapidly and consume high degree of supersaturation at the beginning of condensation, the number of condensed particles is typically much smaller than the number of condensation nuclei and varies over two orders of magnitudes according to the parcel cooling rate. In this study, as a first step, instead of calculating the possible variation, assuming N_* to be constant and homogeneous, we explore the sensitivity of the results to N_*. We employ three widely different values of N_*, which are, 5.0×10^8 kg^{-1}, the value estimated for the present Mars by Tobie et al. (2003), and 5.0×10^6 and 5.0×10^4 kg^{-1}, which Forget et al. (2013) uses referring to the observations of condensation nuclei in Earth's atmosphere (Hudson and Yum 2002; DeMott et al. 2003).

Time integration of each run is performed until we can judge that a statistical equilibrium state is reached. The time step for the terms associated with sound wave and condensation is 0.25 s, and the one for the other terms is 2 s.

4. Results

a. Characteristics of temporal evolutions

Here we overview the results of the runs with $N_* = 5.0 \times 10^6$ kg^{-1}. Figure 2 compares temporal evolutions of total kinetic energy (Figs. 2a,b) and horizontal-mean cloud density (Figs. 2c,d) for the two runs using two different values of S_{cr}. For the case with $S_{cr} = 1.0$, both total kinetic energy and horizontal-mean cloud density reach their respective quasi-stationary values after about 10 days from the start of time integration (Figs. 2a and 2c) except for the existence of small amplitude fluctuations with a temporal scale of several days. For the case with $S_{cr} = 1.35$, in contrast, distinct quasi-periodic burst events characterized by the synchronous increase of total kinetic energy (Fig. 2b) and horizontal-mean cloud density (Fig. 2d) are

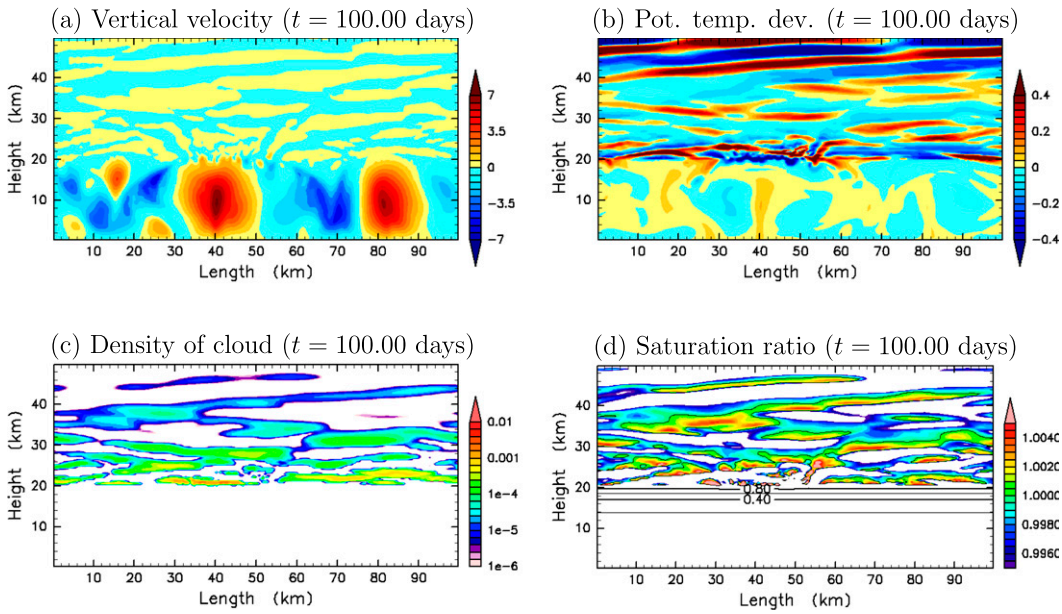

FIG. 3. Spatial distributions of variables at t = 100 days for the case with S_{cr} = 1.0 and $N_* = 5.0 \times 10^6\,\mathrm{kg}^{-1}$. (a) Vertical velocity ($\mathrm{m\,s^{-1}}$), (b) potential temperature deviation from the horizontal mean (K), (c) mass density of CO_2 ice cloud ($\mathrm{kg\,m^{-3}}$), and (d) saturation ratio.

observed. The burst events occur with a time interval of about 15 days and each event lasts only about 3 days. No cloud forms during the periods between the burst events. Total kinetic energy during the burst events is about 5 times as large as that during the cloud-free periods (Fig. 2b).

In the following two subsections, we examine the detailed structures of flow fields and cloud distributions of these two cases. For convenience, we refer to the altitude, 20 km, separating the dry adiabatic layer and the saturated layer in the basic state, as the "condensation level," since the lifting condensation levels for the air parcels from below resides close to this altitude throughout all runs of the experiment. Also for convenience, we refer to the layer from the condensation level to the bottom of the isothermal layer (at about 50-km height) as the "condensation layer."

b. *Case with* S_{cr} = 1.0

Figure 3 shows snapshots of model variables at t = 100 days of the case with S_{cr} = 1.0. Characteristics of the circulation field are distinctly different between the height regions above and below the condensation level. Below the condensation level, cellular convection develops. The updrafts associated with the cellular convection are strongly suppressed at the condensation level and penetrate above it by only about 1 or 2 km, where potential temperature is lower (Fig. 3b) and cloud density is higher (Fig. 3c) in the updrafts, compared with their respective horizontal-mean values. Just below the dense clouds capping the strong updraft in the lower layer, one can find smaller-scale cellular alternating vertical flows, for example, at around x = 40 km in Fig. 3a, whose spatial scale is about 2 km. These are driven by the cooling due to evaporation of falling cloud particles. Horizontal-mean cloud mass density is largest at around the altitude of 21 km (Fig. 2c); about a half of total cloud mass is concentrated in the lowermost 5 km of the condensation layer.

The rest of the condensation layer is characterized by wavelike features. Vertical velocity associated with the wavelike features is as weak as about 0.1 $\mathrm{m\,s^{-1}}$, contrasting with about 5 $\mathrm{m\,s^{-1}}$ of that below the condensation level. The temporal evolution of potential temperature (not shown here) indicates that the phase lines of wavelike features propagate downward, implying that they are of a kind of internal gravity waves. Condensation occurs in the regions where supersaturation develops as a result of the cool anomalies associated with propagation of the wavelike features (Figs. 3b,d). Actually, there emerges restoring buoyancy force associated with vertical displacements of air parcels. One may expect that an air parcel is neutral to a quasi-equilibrium adiabatic displacement in which condensation or evaporation would immediately follow the change of pressure, as the condensation layer is mostly constrained to the saturation temperature structure. However, a descending parcel with no or little condensates follows or approaches dry adiabat and attains positive buoyancy, since the saturation temperature structure is statically stable. An ascending and thus condensing parcel, on the other hand, attains negative buoyancy caused by the drag force of condensates.

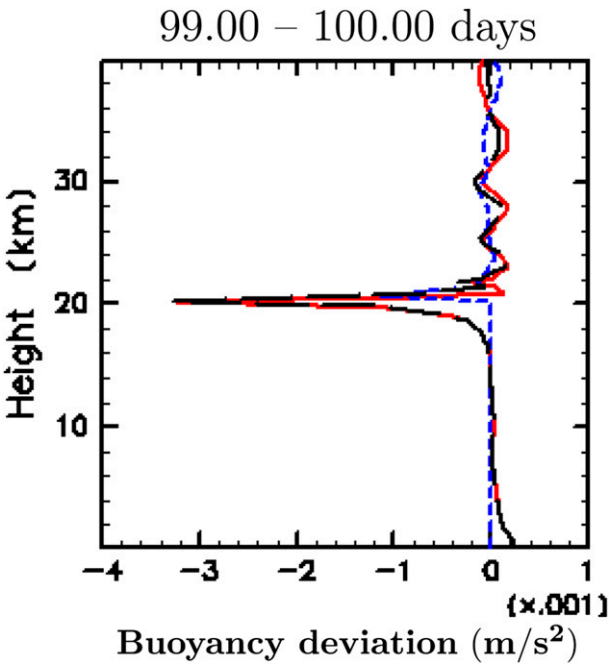

FIG. 4. Vertical profiles of the deviations of acceleration ($\mathrm{m\,s^{-2}}$) due to thermal buoyancy (solid red line), due to drag force of cloud particles (dashed blue line), and due to net buoyancy (black line) from the corresponding horizontal means for the case with $S_{cr} = 1.0$ and $N_* = 5.0 \times 10^6\,\mathrm{kg^{-1}}$. Plotted values have been averaged between $t = 99$ and $t = 100$ days and over an ascending region between $x = 32$ and $x = 46$ km.

Figure 4 shows the vertical profiles of the acceleration due to thermal buoyancy and drag force of cloud particles, which are the second and the third terms of the right-hand side of Eq. (2), respectively, in an ascending region of the convection—namely, averaged over the region between $x = 32$ and $x = 46$ km from $t = 99$ days to $t = 100$ days. Plotted are the deviations from the corresponding horizontal means. Both thermal buoyancy and drag force due to cloud particles have negative peaks at or just above the condensation level, resulting in a distinct negative peak of net buoyancy force near the condensation level, which inhibits the lower-level updrafts from penetrating more than 1 or 2 km. The argument by Colaprete et al. (2003) that an ascending parcel with the condensation of major component does not obtain positive buoyancy is therefore confirmed.

c. *Case with* $S_{cr} = 1.35$

In the case with $S_{cr} = 1.35$, clouds form as distinct quasi-periodic burst events (Figs. 2b and 2d). In the following, we refer to the time periods free from condensation as "noncondensation periods" and the periods with intense condensation as "condensation periods." Figure 5 shows temporal evolutions of vertical velocity and cloud mass density from the beginning to the end of a condensation period.

Just before the condensation period, at $t = 143.50$ days, convective motion is present only below the condensation level (Fig. 5a1), and internal gravity waves develop above the level of condensation, as indicated by potential temperature deviation (Fig. 6a). Cloud mass density is quite low (Fig. 5a2), being well below the threshold value ρ_s^T introduced in condensation–evaporation process. Appreciable supercooling is observed in most parts of the condensation layer (Fig. 6b). Saturation ratio is larger in the lower altitudes, approaching the critical value S_{cr} near the condensation level, as will be described later (Fig. 7b).

The condensation period begins at $t = 143.53$ days, as a cloudy region develops near the condensation level (Figs. 5b1 and b2). The onset of condensation occurs at around $x = 75$ km, just over an ascending region of cellular convection continuing in the lower layer. Once the cloudy region starts to develop, it quickly extends upward, reaching the altitude of 30 km at $t = 143.55$ days (Fig. 5c2). Strong cloudy updrafts are found only near the cloud top (Fig. 5c1), and their intensity is about 2–3 $\mathrm{m\,s^{-1}}$. In spite of the upward cloud development, the location of maximum cloud density remains just above the condensation level. The peak value of cloud mass density, $1.0 \times 10^{-2}\,\mathrm{kg\,m^{-3}}$, is about four times as large as that in the case of $S_{cr} = 1.0$. In the cloud, potential temperature is nearly equal to saturation potential temperature, being higher than that of the surrounding supercooled regions (Fig. 6c). Note that saturation ratio around the cloud top is smaller than S_{cr} (Fig. 6d), implying that the condensation at the cloud top occurs not because saturation ratio exceeds S_{cr} but because cloud particles of density exceeding ρ_s^T are advected from the below. After 3 h from the beginning of the condensation period, at $t = 143.63$ days, the cloud thickens further and reaches the top of the condensation layer, but vertical velocity weakens (Figs. 5d1 and 5d2). Subsequently, the cloud extends horizontally, decaying with gravitational settling of cloud particles (Figs. 5e1 and 5e2), and disappears completely in 3 days from the beginning of the active period (Figs. 5f1 and 5f2).

A noteworthy characteristic of the cloud is that deep vertical flow penetrating through the entire condensation layer does not develop at any moment of the condensation periods, in contrast to that of updrafts associated with cumulonimbi in Earth's atmosphere. In the case of Earth's clouds, where a minor component, water vapor, condenses at $S \sim 1$ upward motion and latent heating due to condensation couples basically in a linear fashion. Namely, once an air parcel begins to move upward by condensation heating, air parcels below and above it are also lifted upward because of

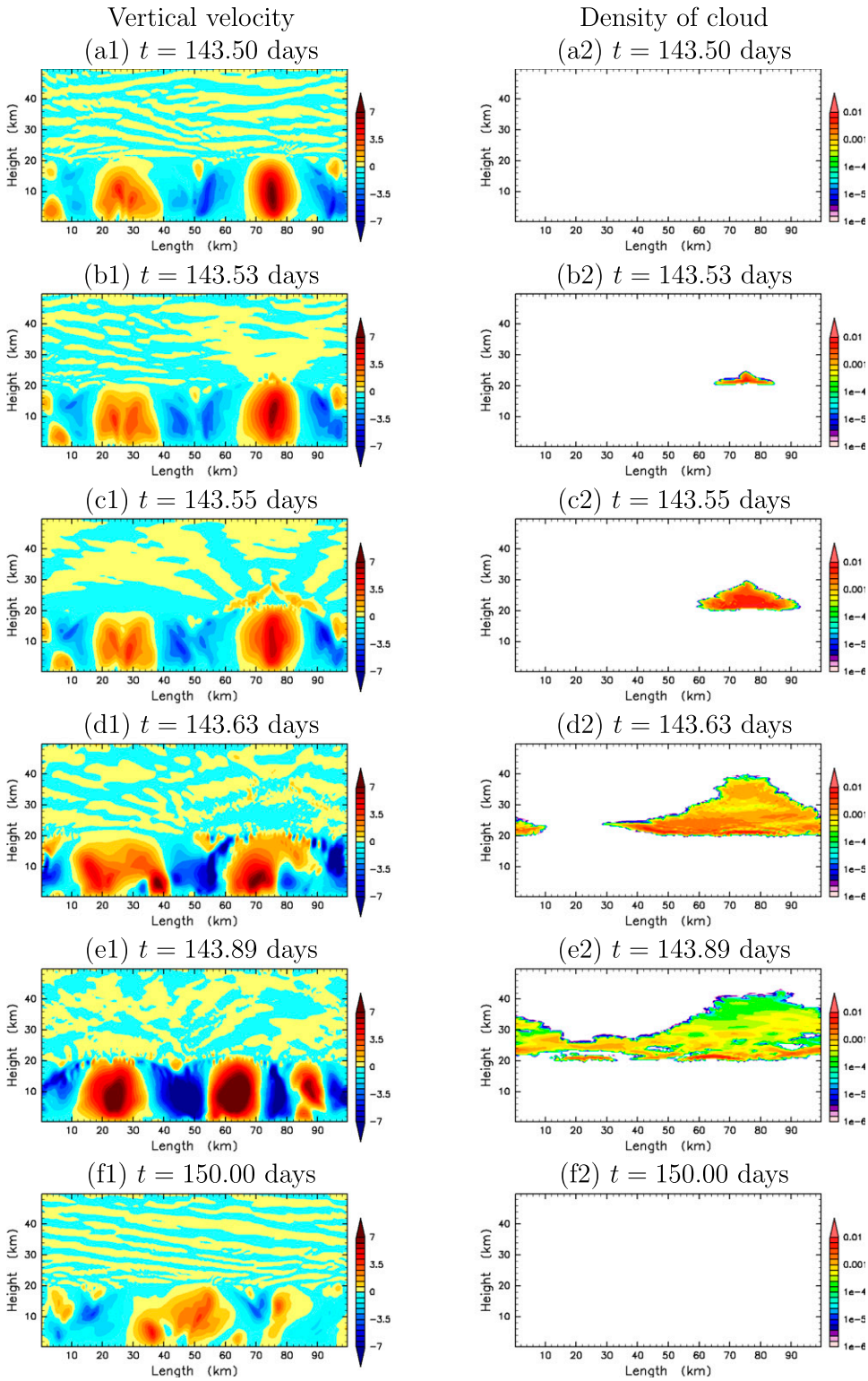

FIG. 5. Spatial distributions of (a1)–(f1) vertical velocity ($\mathrm{m\,s^{-1}}$) and (a2)–(f2) mass density of CO_2 ice cloud ($\mathrm{kg\,m^{-3}}$) for the case with $S_{cr} = 1.35$ and $N_* = 5.0 \times 10^6\,\mathrm{kg^{-1}}$ at (top to bottom) t = 143.50, 143.53, 143.55, 143.63, 143.89, and 150.0 days, respectively. Note that the time of (a) is equal to that of Figs. 6a,b and that of (c) is equal to that of Figs. 6c,d.

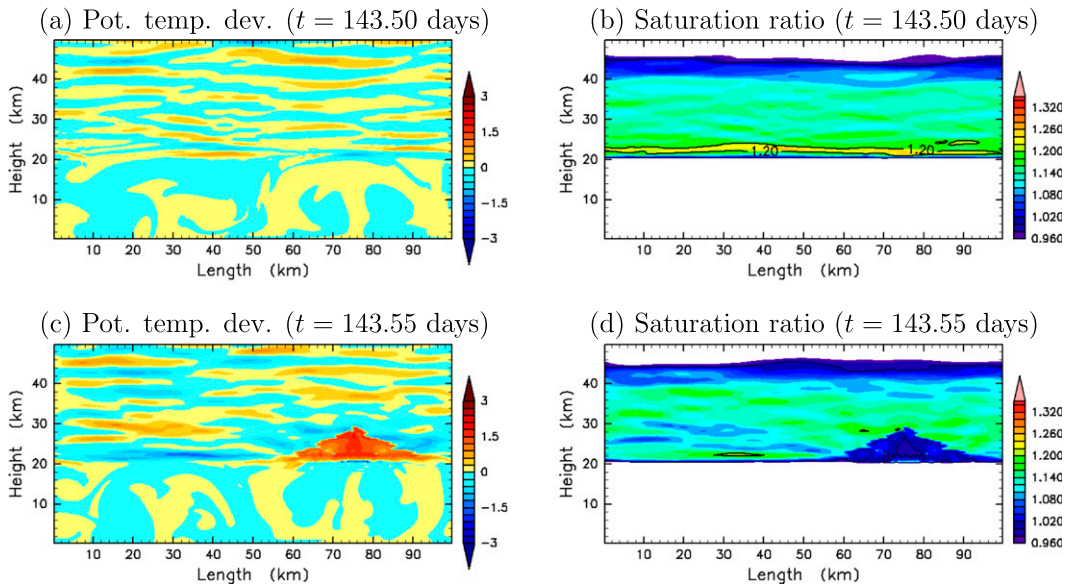

FIG. 6. Spatial distributions of (a),(c) potential temperature deviation from the horizontal mean (K) and (b), (d) saturation ratio in the case with $S_{cr} = 1.35$ and $N_* = 5.0 \times 10^6\,\mathrm{kg}^{-1}$ at (a),(b) $t = 143.50$ days, near the end of the noncondensation period, and (c),(d) $t = 143.55$ days in the early stage of the condensation period.

continuity, where condensation also starts inducing positive buoyancy in these parcels. Such a ''chain reaction'' results in vertical development of positively buoyant columns extending the whole depth of the moist unstable layer. In contrast, upward motion and latent heating due to condensation are almost unrelated in the present case. Once condensation becomes switched on when either of the thresholds of the degree of supersaturation or the amount of condensates is overcome, condensation proceeds very quickly to reach the saturated state, almost irrespective of the intensity or signature of the vertical motion. Further, after the saturated state is achieved, positive buoyancy can no longer be generated even if condensation proceeds, because the temperature structure is now constrained by the saturation profile. Because of the decoupling between vertical motion and buoyancy generation, no chain reaction leading to the downward development and maintenance of upward motion occurs, and hence a strong updraft exists only in the thin layer at the top of a convective cloud.

Figure 7 shows temporal evolutions of the vertical profiles of horizontal-mean cloud mass density and horizontal-mean temperature at $z = 22.2$ km, just above the condensation level, covering multiple condensation events including the one described above. During the short periods when clouds grow upward, the horizontal-mean temperature near the condensation level rapidly approaches saturation temperature, and in the following periods of about 3 days, during which cloud mass density decreases, horizontal-mean temperature is kept nearly equal to saturation temperature. After cloud particles fall off completely from the condensation layer, a noncondensation period begins. It continues about 15 days, during which horizontal-mean temperature decreases monotonically toward the value that corresponds to critical saturation ratio just before the next condensation period. In the repeated cycles of condensation and noncondensation periods, horizontal-mean temperature in the condensation layer evolves in a sawtoothlike curve.

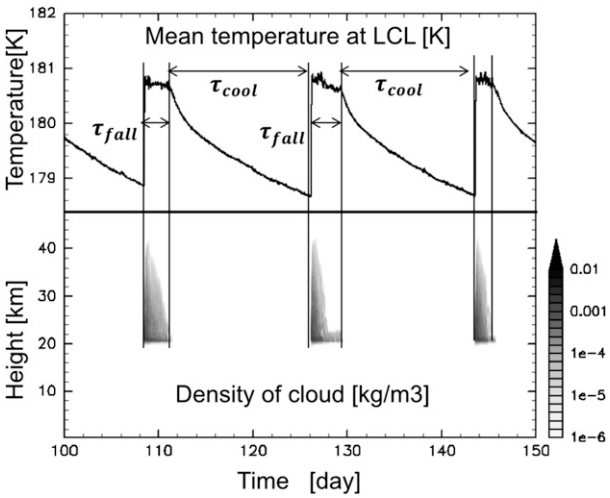

FIG. 7. (top) Time evolution of the horizontal-mean temperature (K) near condensation level ($z = 22.2$ km) and (bottom) the vertical distribution of the horizontal-mean mass density ($\mathrm{kg\,m^{-3}}$) of CO_2 ice cloud from $t = 100$ to 150 days in the case with $S_{cr} = 1.35$ and $N_* = 5.0 \times 10^6\,\mathrm{kg}^{-1}$. The quantities τ_{fall} and τ_{cool} are the time scales of gravitational settling and radiative cooling, respectively (see text).

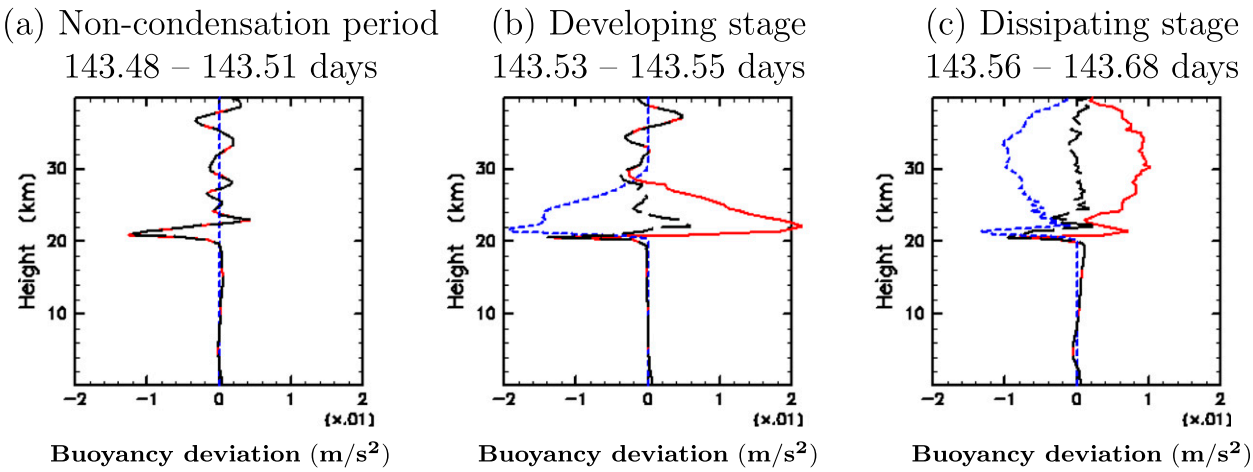

FIG. 8. Vertical profiles of the deviations of the accelerations due to thermal buoyancy (solid red line), due to drag force (dashed blue line), and due to net buoyancy (black line) from the corresponding horizontal means (m s^{-2}) for the case with $S_{cr} = 1.35$ and $N_* = 5.0 \times 10^6$ kg^{-1}. (a) Last stage of noncondensation period averaged from $t = 143.48$ to 143.51 days, (b) early stage of condensation period averaged from $t = 143.53$ to 143.55 days, and (c) later stage of condensation period averaged from $t = 143.56$ to 143.68 days. Plotted are values averaged in an ascent region between $x = 70$ and $x = 80$ km.

Although the structure of dry convective motion below the condensation level does not seem to change in the entire cycle, its intensity varies. The convection is most intense when clouds finish growing in the condensation layer in the middle of the condensation periods; vertical velocity at that time (Fig. 5e1) is about twice as intense as that at the beginning of condensation period (Fig. 5b1). This enhancement of convection is induced by evaporation of cloud particles falling from the clouds developing intensively above, which cools the top of the dry convective layer below, resulting in the synchronization of the temporal evolutions of total kinetic energy (Fig. 2b) and cloud formation (Fig. 2d).

Thermal buoyancy force, drag force due to cloud particles, and net buoyancy force, which is the sum of the two, in an ascending region during three different periods of cloud growth are plotted in Figs. 8a–c. Plotted are the deviations from the corresponding horizontal means. Before the condensation period (Fig. 8a), the profiles are similar to those in the case with $S_{cr} = 1.0$ (Fig. 4) except that the contribution from drag force is absent. During the condensation period (Figs. 8b and 8c), the deviation of thermal buoyancy force is always positive in the condensation layer, whereas the deviation of drag force is always negative. In the stage of upward cloud development, the deviation of net buoyancy force is positive in the ascending cloudy region (Fig. 8b). This is because temperature in the condensing region is nearly at saturation, whereas the clear environment is supercooled and, hence, the large difference in potential temperature between the cloud region and the surroundings is allowed (Fig. 6c). Note that a considerable portion of the buoyancy gained by temperature deviation is canceled by drag force, resulting in only modest vertical velocity (Figs. 5c1 and 5c2). In the cloud dissipation stage, net buoyancy deviation becomes negative (Fig. 8c), as the temperature difference between the cloud region and the environment becomes smaller, leading to the extinction of the updrafts in the condensation layer. The temperature rise outside of the cloud is mainly caused by adiabatic heating associated with compensating subsidence and advection of warm air from the cloud region (not shown).

5. Sensitivity to number mixing ratio of condensed particles

In this section, we will examine dependence of convective motion and cloud distribution on the value of number mixing ratio of condensed particles, N_*, which we introduce as a parameter given externally, since a possible range of N_* in the early Martian atmosphere is hardly known. The value of N_* controls the size of individual cloud particles, which determines their fall velocity, and hence is expected to influence flow field and cloud distribution.

Figure 9 shows temporal evolutions of the vertical profiles of horizontal-mean cloud mass density for the cases with various values of N_*. As for the cases with $S_{cr} = 1.0$, quasi-steady solutions are obtained regardless of the value of N_* (Figs. 9a,c). The spatial structure of convective motion is not very sensitive to the value of N_* (figure not shown). However, as is indicated in Figs. 10a–c, the amount of cloud mass depends on the value of N_*; the total and the maximum values of cloud mass density decrease as the decrease of N_*. As for the cases with $S_{cr} = 1.35$, the characteristics of the distribution of horizontal-mean cloud mass density depend strongly on the value of N_*; a quasi-periodic solution appears also for $N_* = 5.0 \times 10^4$ kg^{-1} (Fig. 9b),

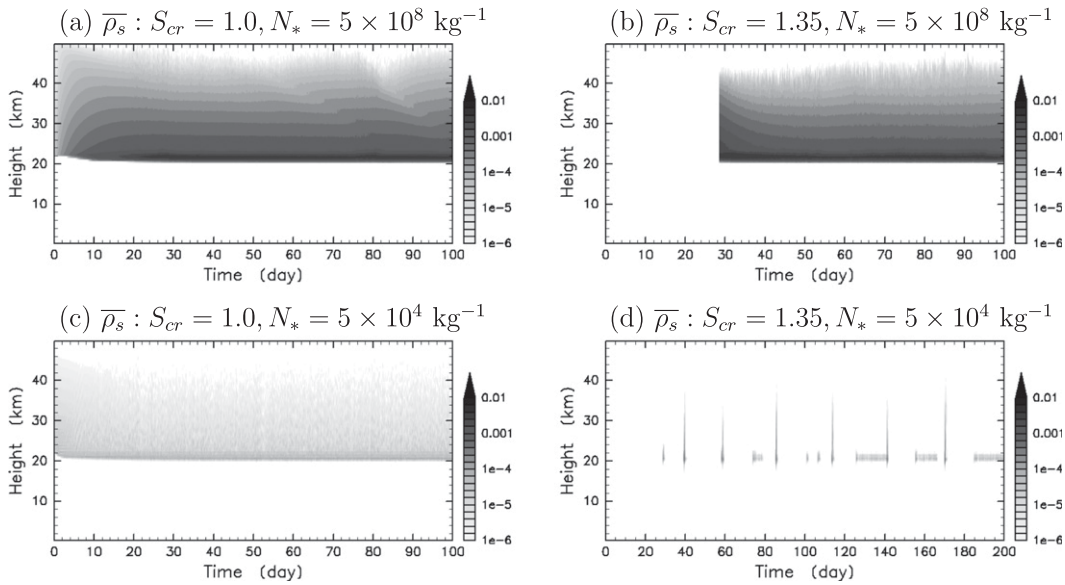

FIG. 9. As in Figs. 2c,d, but with (a),(b) $N_* = 5.0 \times 10^8$ and (c),(d) $N_* = 5.0 \times 10^4\,\mathrm{kg}^{-1}$.

while for $N_* = 5.0 \times 10^8\,\mathrm{kg}^{-1}$ (Fig. 9d), a quasi-steady solution is obtained, whose spatial structure (Fig. 10d) is similar to those in the cases of $S_{\mathrm{cr}} = 1.0$.

A close examination reveals some difference between the two quasi-periodic solutions obtained for $S_{\mathrm{cr}} = 1.35$ with the smaller two values of N_*. As described in section 4c, in the case of $N_* = 5.0 \times 10^6\,\mathrm{kg}^{-1}$, a cloud always emerges just above the condensation level and grows upward, accompanied with upward flow near the cloud top. In the case of $N_* = 5.0 \times 10^4\,\mathrm{kg}^{-1}$, on the other hand, two different types of cloud development can be identified; one type emerges as shallow stratiform clouds just above the condensation level (Fig. 11a), while the other type emerges as localized patch-like clouds in the upper part of the condensation layer, above the height of 30 km (Fig. 11b). Neither of the two types of clouds grows upward. The former type of clouds emerge just above the condensation level (Fig. 11a) and keep their altitudes appearing as the more or less persistent areas of large cloud mass density around the condensation level in Fig. 9d. The latter type of clouds develops downward (Figs. 11b–d) with their cloud density increasing. These two types of clouds do not necessarily develop simultaneously. The clouds just above the condensation level emerge more frequently and irregularly, while the clouds in the upper part of the condensation layer appear less frequently but quasi periodically (Fig. 9d). Once such a high origin cloud develops, similar downward developing clouds appear one after another (Fig. 11e) and cover a large part of the condensation layer. Because of the associated latent heat release, there occurs rapid temperature increase throughout the condensation layer (figure not shown), which characterizes the condensation periods. Therefore, in spite of the difference in the behaviors of clouds between the cases of $N_* = 5.0 \times 10^6$ and $N_* = 5.0 \times 10^4\,\mathrm{kg}^{-1}$, they resemble each other in their gross temporal evolutions of horizontal-mean cloud density and total kinetic energy (not shown here).

The sensitivities of flow field and cloud distribution to N_* result from the dependence of terminal velocity of cloud particles on N_*. For the same cloud mass density, cloud particle radius is larger for the case with smaller N_* [Eq. (11)] and, hence, terminal velocity is larger [Eq. (16)]. In the case of $N_* = 5.0 \times 10^6\,\mathrm{kg}^{-1}$, the calculated maximum value of vertical velocity in the condensation layer and the value of terminal velocity of cloud particles are about 3 and $0.6\,\mathrm{m\,s}^{-1}$, respectively, implying that cloud particles can be transported upward, and they trigger condensation at cloud top, and hence clouds develop upward as seen in Fig. 5. Moreover, since the residence time of cloud particles in the condensation layer is fairly long, condensation continues until saturation ratio almost reaches unity. In contrast, in the case of $N_* = 5.0 \times 10^4\,\mathrm{kg}^{-1}$, the calculated maximum value of vertical velocity in the condensation layer and the value of terminal velocity of cloud particles are about 0.5 and $6\,\mathrm{m\,s}^{-1}$, respectively, implying that cloud particles cannot be transported upward but fall down, so clouds cannot grow upward. Moreover, because of the quick loss of cloud particles from the condensation layer, condensation cannot proceed to achieve saturation ratio of nearly unity. In fact, the value of saturation ratio in the upper portion of the condensation layer remains considerably larger than unity throughout the entire integration period. Condensation in the upper part of the condensation layer

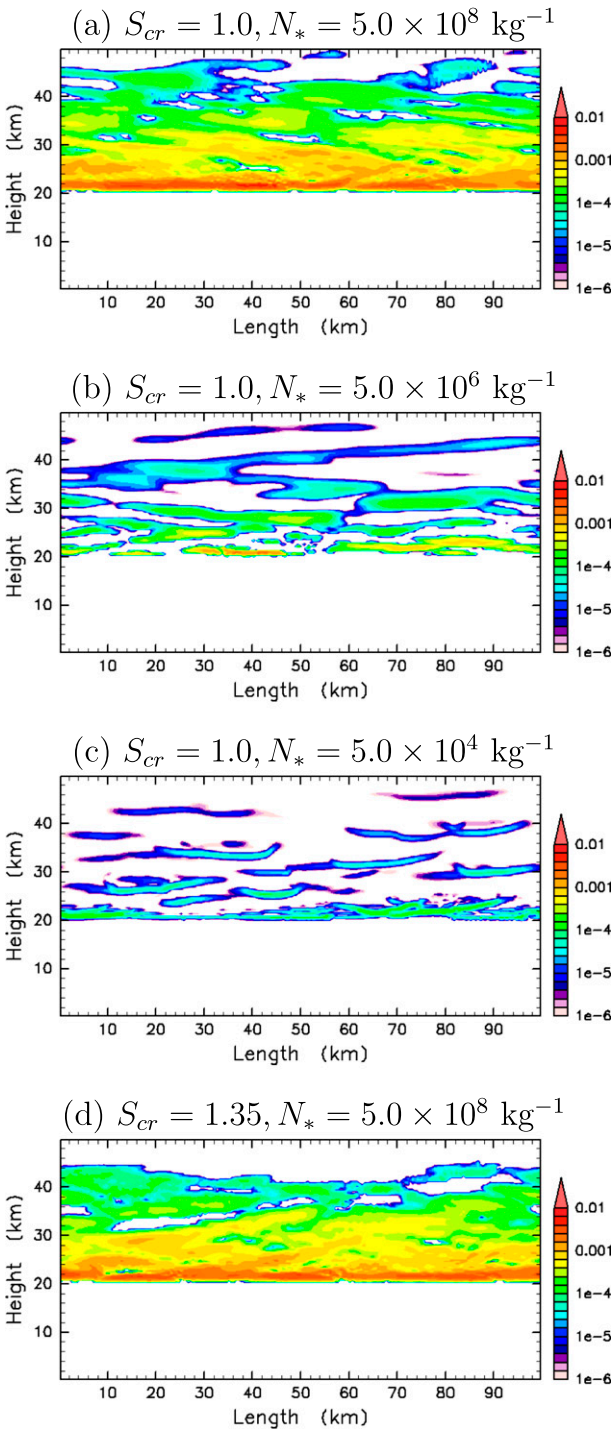

FIG. 10. Spatial distributions of mass density (kg m^{-3}) of CO_2 ice cloud at $t = 100$ days in the cases with $S_{cr} = 1.0$ and (a) $N_* = 5.0 \times 10^8$, (b) $N_* = 5.0 \times 10^6$, and (c) $N_* = 5.0 \times 10^4$ kg^{-1}, and with (d) $S_{cr} = 1.35$ and $N_* = 5.0 \times 10^8$ kg^{-1}.

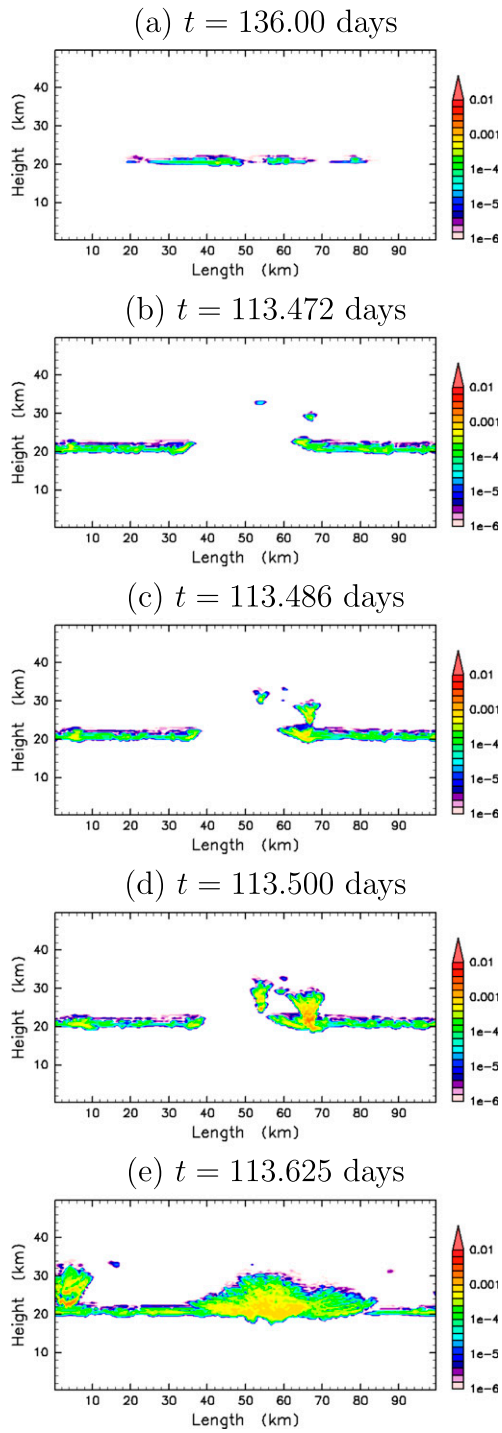

FIG. 11. Spatial distributions of mass density (kg m^{-3}) of CO_2 ice cloud for the case with (a) $S_{cr} = 1.35$ and $N_* = 5.0 \times 10^4$ kg^{-1} during the period with clouds restricted around the condensation level ($t = 136.00$ days) and with (b)–(e) those developing in higher altitudes ($t \sim 113.5$ days).

starts only after the layer is cooled to attain S_{cr}, which is first satisfied at around $z = 30$ km in the present case, resulting in condensation there, and clouds develop downward owing to the gravitational sedimentation.

6. Discussions

a. Periodicity caused by permitting supersaturation

Summarizing the results in the previous two sections, quasi-periodic solutions are obtained when S_{cr} is considerably larger than unity and N_* is small enough, while quasi-steady solutions are obtained otherwise. In the case of quasi-periodic solution, temporal evolution in the condensation layer is characterized by alternating short condensation periods and long noncondensation periods (Figs. 2 and 9), implying that the intermittency of condensation results from the quick termination of the condensation periods.

For $S_{cr} > 1$, when the saturation value is below S_{cr}, condensation should cease if the cloud particles are lost by gravitational sedimentation and ρ_s falls below ρ_s^T (see Fig. 7a). Thus the duration of the condensation period can be estimated by the time scale of gravitational sedimentation of cloud particles τ_{fall}, which can be evaluated with the depth of the condensation layer D_{cloud} and the terminal fall velocity of cloud particles. From Eqs. (16) and (11), assuming that $r_c \gg r_{as}$, τ_{fall} can be expressed as

$$\tau_{fall} \sim D_{cloud}/V_{term} \sim \frac{9\eta D_{cloud}}{2g\rho_I}\left(\frac{4\rho_I\pi\rho}{3\rho_s}\right)^{2/3} N_*^{2/3}, \tag{20}$$

neglecting the Cunningham correction.

To proceed with the further evaluation of Eq. (20), density of cloud particles, ρ_s, must be estimated. Two estimations of ρ_s are possible. One is ρ_s^T, which can be proposed as the lower limit of ρ_s, leading to the upper limit of the duration of condensation period. The other is the amount of cloud mass given by quasi-static condensation of supercooled parcels estimated as below, which can be proposed as an upper limit of ρ_s, leading to the lower limit of the duration of condensation period. Let us consider condensation of a supersaturated air parcel whose temperature and saturation ratio are T and $1 + \Delta S$, respectively, neglecting the change in pressure, which is assumed to adjust quickly to the surroundings. Using the Clausius–Clapeyron equation and neglecting the volume of condensates, temperature rise after condensation, ΔT (see Fig. 7b), satisfies

$$\begin{aligned}(1+\Delta S)p^*(T) &= p^*(T+\Delta T) \sim p^*(T) + \frac{\partial p^*}{\partial T}\Delta T \\ &= p^*(T)\left(1 + \frac{L}{RT^2}\Delta T\right),\end{aligned}$$

giving

$$\Delta T \sim \frac{RT^2}{L}\Delta S. \tag{21}$$

Since ΔT is supplied by condensation heating, density of cloud mass produced by condensation, ρ_s^S, can be related as

$$\rho c_p \Delta T = L\rho_s^S. \tag{22}$$

Combining the above two relations, we can estimate mass density of cloud particles, neglecting gravitational sedimentation, as

$$\rho_s^S \sim \frac{c_p RT^2}{L^2}\rho\Delta S. \tag{23}$$

Note that the numerical value of the factor in the rhs, $c_p RT^2/L^2$, is as small as 1/50; ρ_s^S is considerably smaller than a naive estimation, $\rho\Delta S$.

If we employ the condition just above the condensation level, where temperature and density are 183 K and 0.915 kg m^{-3}, respectively, and assume $\Delta S = S_{cr} - 1 = 0.35$, Eq. (23) yields 5.1×10^{-3} kg m^{-3} as the estimated value of ρ_s^S, which is about a half of the amount of condensate realized at the beginning of the condensation period in the case of $N_* = 5 \times 10^6$ kg^{-1}, which reaches 1×10^{-2} kg m^{-3} (see Fig. 5b). This moderate discrepancy could be explained by the accumulation of cloud particles through a possible balance between gravitational sedimentation and upward advection. On the other hand, the value of ρ_s realized in the run with $N_* = 5 \times 10^4$ kg^{-1}, about 3×10^{-4} kg m^{-3} (see Fig. 11b), is an order of magnitude smaller than the estimate of ρ_s^S above. This is presumably because, due to rapid gravitational sedimentation, cloud particles are lost before condensation proceeds to the non-oversaturated state.

Now we can obtain upper and lower limits of τ_{fall}, by substituting ρ_s^T and ρ_s^S in Eq. (23) for ρ_s in Eq. (20), respectively. Further assuming that the supersaturation value is $\Delta S = S_{cr} - 1 = 0.35$, and that D_{cloud} is 10^4 m, the depth scale of intermittent clouds that develop in the experiments (see Fig. 5), we have $2 \times 10^4 \lesssim \tau_{fall} \lesssim 5 \times 10^6$ s for $N_* = 5 \times 10^6$ kg^{-1}. As described in section 4c, the typical duration of the condensation periods is about 3 days, or 3×10^5 s, which is in the middle of the estimated range of τ_{fall}, suggesting that the duration of the condensation period is presumably governed by the removal due to gravitational sedimentation. With $N_* = 5 \times 10^4$ kg^{-1}, we have 1×10^3 s $\lesssim \tau_{fall} \lesssim 2 \times 10^5$ s. As ρ_s is one order of magnitude smaller than ρ_s^S as noted above, the fall time realized in the model should be longer than the lower limit, but the estimated upper limit assures quick termination of condensation events.

After condensation is terminated in reasonably short time interval, the temporal evolution of temperature in the condensation layer is governed exclusively

by radiative cooling (body cooling). Then, the sawtoothlike quasi-cyclic variation of temperature appears (Fig. 7b), whose period can be estimated by $\tau_{\rm cool} \sim \Delta T/Q_{\rm rad}$, where $Q_{\rm rad}$ is cooling rate and ΔT is the temperature rise during the condensation periods. We should note, however, that Eq. (20) gives a long but finite time as the estimate of $\tau_{\rm fall}$ even for arbitrary large value of N_* and cannot explain seemingly everlasting cloud development in the case with $N_* = 5 \times 10^8\,{\rm kg}^{-1}$. In the case with large N_*, it is presumably internal gravity waves ubiquitous in the condensation layer that contribute to the persistent generation of clouds by incessantly shaking up and down every portion of the condensation layer.

b. *Vertical profiles of cloud mass density in quasi-steady solutions*

As is shown in Figs. 10a–c, the vertical profiles of cloud mass density in the quasi-steady solutions obtained in the cases of $S_{\rm cr} = 1.0$ depend strongly on N_*. In the following, we quantitatively consider the origin of the sensitivity to N_*. As a preparation, we examine the heat and the cloud mass budgets in the condensation layer in the case with $S_{\rm cr} = 1.0$ and $N_* = 5.0 \times 10^6\,{\rm kg}^{-1}$. In the upper part of the condensation layer (z = 25–50 km), radiative cooling nearly balances with condensation heating in the potential temperature budget (Fig. 12a), and condensation nearly balances with gravitational settling in the cloud mass density budget (Fig. 12b). In the lower part of the condensation layer (z = 20–25 km), the sum of advection and turbulent diffusion nearly balances with latent heating in the potential temperature budget (Fig. 12c). Note that the sign of each term flips at the condensation level. In the cloud mass density budget, the sum of advection and turbulent diffusion does not balance with condensation–evaporation (Fig. 12d); the difference between condensation–evaporation and the sum of advection and turbulent diffusion is compensated by gravitational settling.

Based on the characteristics of heat and cloud mass density budgets summarized above, we can understand the dependence of the horizontal-mean vertical distribution of cloud mass density on N_*. For simplicity, we assume horizontally uniform distributions of potential temperature and cloud density. Combining the balance between condensation heating and radiative cooling (Figs. 12a,b),

$$\frac{LM_{\rm cond}}{\overline{\rho} c_p} \approx -Q_{\rm rad}, \tag{24}$$

and the cloud mass density balance between condensation and gravitational settling,

$$\frac{d}{dz}(\rho_s V_{\rm term}) \approx -M_{\rm cond}, \tag{25}$$

we have

$$\frac{d}{dz}(\rho_s V_{\rm term}) \approx \frac{\overline{\rho} c_p Q_{\rm rad}}{L}. \tag{26}$$

Estimating $V_{\rm term}$ from Eq. (16), using the size of cloud particles from Eq. (11) and Cunningham correction from Eq. (18) which can be nonnegligible above the altitudes of ~30 km, we obtain an expression

$$\frac{d}{dz}\left\{\frac{2g\rho_I\rho_s}{9\eta}\left(\frac{3\rho_s}{4\rho_I\pi\overline{\rho}N_*}\right)^{1/3}\left[\left(\frac{3\rho_s}{4\rho_I\pi\overline{\rho}N_*}\right)^{1/3}+\frac{4}{3}\lambda\right]\right\} = \frac{\overline{\rho} c_p Q_{\rm rad}}{L}. \tag{27}$$

By numerically integrating Eq. (27) from an altitude z in the condensation layer to the top of the layer and with a few additional algebraic manipulations, we can obtain an estimate of ρ_s as a function of z for the most of the condensation layer except for the region just around the condensation level.

In the lower portion of the condensation layer (below about 23 km), which is affected by the mixing from below caused by the penetration of dry convection, the balance of Eq. (26) is not realized. A better starting point is to find a parcel-conserved thermodynamic quantity. In reality, gravitational sedimentation plays a nonnegligible role, but we disregard it for simplicity. Then, the sum of enthalpy, gravitational potential energy, and latent heat of deposition–sublimation of CO_2 with the sign reversed (i.e., $c_pT + gz - L\rho_s/\rho$) is conserved. This corresponds to the liquid water static energy often used for Earth's atmosphere where the condensate is liquid H_2O (Betts 1975), so we refer to it as "CO_2 ice static energy" below. In each of the cases with $S_{\rm cr} = 1.0$ and in the case with $S_{\rm cr} = 1.35$ and $N_* = 5 \times 10^8\,{\rm kg}^{-1}$, for which a quasi-steady solution is realized, CO_2 ice static energy is observed to be homogenized from the ground surface to about 21 km (not shown). Then, equating the value of CO_2 ice static energy at an altitude z to that at the condensation level $z_{\rm LCL}$, where $\rho_s = 0$, we have

$$c_pT(z) + gz - L\rho_s/\rho = c_pT(z_{\rm LCL}) + gz_{\rm LCL}. \tag{28}$$

And, using the ideal gas equation of state and recalling that pressure is equal to saturation vapor pressure in the condensation layer, we have an estimate of the vertical profile of ρ_s for the layer just above LCL as

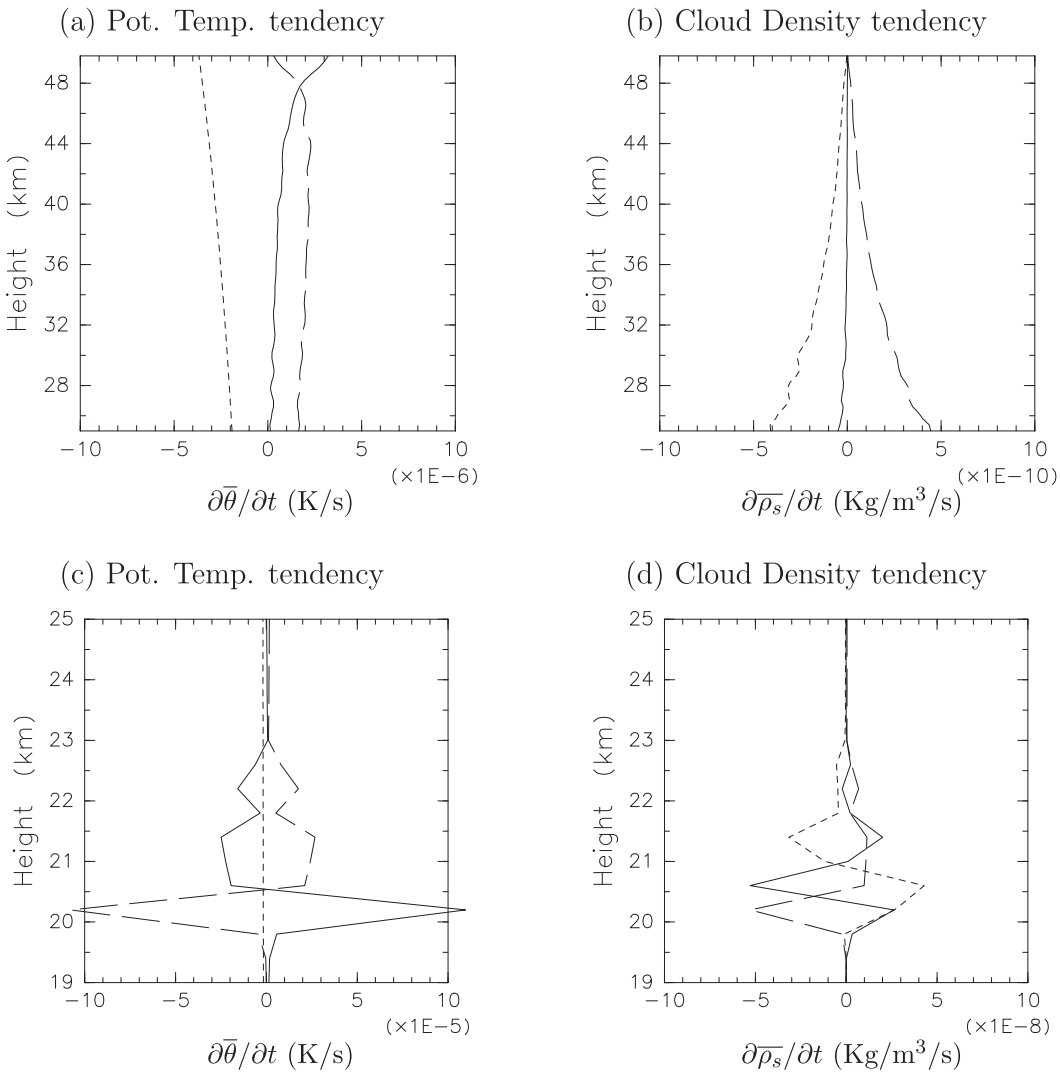

FIG. 12. Horizontal-mean tendencies of (a),(c) potential temperature (K) and (b),(d) cloud mass density (kg m^{-3} s^{-1}) averaged over the period between $t = 90$ and $t = 100$ days in the case with $S_{cr} = 1.0$ and $N_* = 5.0 \times 10^6$ kg^{-1}. The altitudinal region from 25 to 50 km is shown in (a),(b) and that from 19 to 25 km in (c),(d). In (a),(c), plotted are the sum of the advection term and the turbulent diffusion term (solid line), the condensation heating term (line with long dashes), and the radiative cooling term (line with short dashes). In (b),(d), plotted are the sum of the advection term and the turbulent diffusion term (solid line), the condensation term (line with long dashes), and the gravitational settling term (line with short dashes).

$$\rho_s(z) = \frac{\rho(z)}{L}\{c_p[T(z) - T(z_{\mathrm{LCL}})] + g(z - z_{\mathrm{LCL}})\}$$
$$= \frac{p_*[T(z)]}{LRT(z)}\{c_p[T(z) - T(z_{\mathrm{LCL}})] + g(z - z_{\mathrm{LCL}})\}, \tag{29}$$

with the temperature profile

$$T(z) = T(z_{\mathrm{LCL}})\mathrm{e}^{-(g/L)(z - z_{\mathrm{LCL}})}, \tag{30}$$

obtained by integrating the relation $dT(z)/dz = -gT(z)/L$ based on the hydrostatic relation and the Clausius–Clapeyron equation.

Figure 13 shows the profiles of horizontally and time-averaged cloud mass density for the cases with $S_{cr} = 1.0$ (solid line) and those of the two estimates of cloud density; that is, the estimates obtained with Eq. (27) (dotted line) and the estimates obtained with Eq. (29) (dashed line) employing the variables at the cloud base obtained by the corresponding numerical runs as z_{LCL} and $T(z_{\mathrm{LCL}})$. The vertical profile of cloud mass density is well explained by the profile from Eq. (29) below the peak of cloud mass density and by that from Eq. (27) above it. We note, in particular, that the estimate with Eq. (27) succeeds in explaining the strong dependence of cloud density (note the different scales of abscissas of

Figs. 13a–c) on number mixing ratio of condensed particles, N_*, which arises from N_* in the denominators in the two factors on the left-hand side of Eq. (27).

A closer look at Fig. 13 reveals discrepancy between the estimated values of cloud density and the results of numerical experiments, which is more noticeable for the smaller value of N_* reaching to a factor of about 2. The reason for the discrepancy near the condensation level can be easily understood considering the gravitational settling of cloud particles, which is more prominent in the smaller N_* case where the particle sizes tend to be the larger. The reason for the discrepancy in the middle and upper regions of the condensation layer may be attributable to the nonuniformity of cloud density, for which particles in the denser part of cloud are larger in size and have faster terminal fall velocities [cf. Eqs. (11) and (16)], resulting in the reduction of total amount of cloud mass.

The above argument also applies to the case with $S_{\rm cr} = 1.35$ and $N_* = 5.0 \times 10^8\,{\rm kg}^{-1}$, where, owing to slow fall velocities of particles, the value of cloud mass density continuously retains above the condensation threshold and a quasi-steady solution with ceaseless condensation is realized. In fact, the vertical profile of horizontally and time-averaged cloud mass density in this case is nearly the same as that in the case with $S_{\rm cr} = 1$ and $N_* = 5.0 \times 10^8\,{\rm kg}^{-1}$ (not shown here). The same argument cannot be applied to cases with smaller values of N_*, where cloud activity is intermittent and the balance (26) does not hold.

7. Concluding remarks

We have numerically investigated the qualitative characteristics of flow field and cloud distribution associated with condensing convection of a CO_2 atmosphere under an idealized setup with the situation of early Mars in mind. Critical saturation ratio $S_{\rm cr}$ and number mixing ratio of condensed particles N_* are given externally as control parameters. In the case of $S_{\rm cr} = 1.0$, a quasi-steady solution is obtained irrespective of the value of N_*, in which cellular dry convection appears below the condensation level, and dense clouds form near the condensation level by penetrative updrafts associated with the dry convection. An air parcel cannot obtain positive thermal buoyancy in the condensation layer; thus, updrafts penetrate into the condensation layer by only about 1 or 2 km. In the case of $S_{\rm cr} = 1.35$, characteristics of cloud convection depends on N_*. For $N_* = 5 \times 10^6\,{\rm kg}^{-1}$, a quasi-periodic solution where short periods of intense condensation appear repeatedly is obtained. During the periods when condensation does not occur, the flow field is similar to the case with $S_{\rm cr} = 1.0$. On the other hand, during the periods when condensation

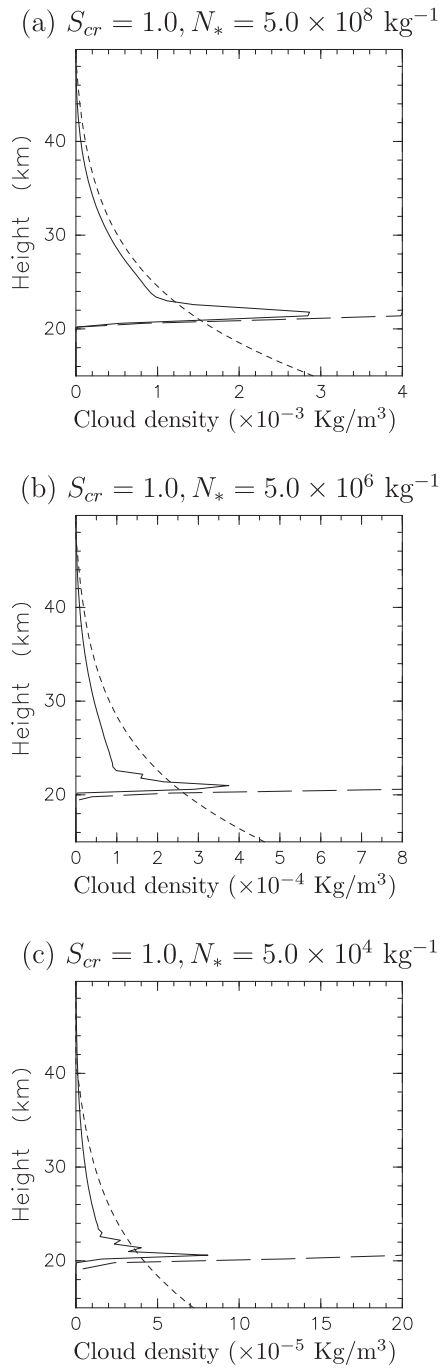

FIG. 13. Time- and horizontal-mean mass density of CO_2 ice cloud obtained by simulation (solid line), mass density of CO_2 ice cloud obtained under the assumption of constant CO_2 ice static energy (line with long dashes), and that obtained under the assumption of the balance of condensation and gravitational settling and the balance of condensation heating and horizontally uniform cooling (line with short dashes) for the cases with (a) $N_* = 5.0 \times 10^8$, (b) $N_* = 5.0 \times 10^6$, and (c) $N_* = 5.0 \times 10^4\,{\rm kg}^{-1}$. All cases shown here are of $S_{\rm cr} = 1.0$, and simulation data are averaged over the period between $t = 110$ and $t = 120$ days.

occurs, dense clouds form in the condensation layer, and updrafts of the magnitudes of 2–3 $m\,s^{-1}$ appear near the top of the clouds. These intense updrafts are driven by the thermal buoyancy that a condensing air parcel can obtain in the supercooled environment. However, thermal buoyancy force is canceled out by drag force due to cloud particles, and accordingly, the strong updrafts appear only around the cloud tops; columnar updrafts penetrating throughout the condensation layer like those of Earth's cumulonimbi do not develop. The quasi periodicity of condensation appears when terminal velocity of cloud particles is large enough that cloud particles are smoothly removed from the condensation layer, and accordingly the atmosphere evolve into the condition of supercooling. For $N_* = 5 \times 10^4\,kg^{-1}$, condensation occurs quasi periodically as in the cases above, but the updrafts associated with condensation are much weaker. For $N_* = 5 \times 10^8\,kg^{-1}$, a quasi-steady solution similar to the cases with $S_{cr} = 1$ develops. It is interesting to note that Colaprete and Toon (2003) also obtained variation of cloud amount with a frequency of several days. However, the mechanisms behind the cloud variations in the present model and theirs are different: in Colaprete and Toon (2003), the variation is associated with the cycle of supply and consumption of aerosols, which is not considered in the present model.

Based on average cloud density profiles achieved in the experiments, we can obtain rough estimates of the radius of cloud particles using Eq. (11) and cloud optical depth employing a simple method [Eqs. (7.67) and (7.71) in Petty (2006)]. Among the cases we examined, only the case with $S_{cr} = 1$ and $N_* = 5 \times 10^{-4}\,kg^{-1}$ provides a combination of particle radius (35 μm) and cloud optical thickness ($\tau \sim 5$), which is within the range favorable for scattering greenhouse effect (Mischna et al. 2000; Forget et al. 2013; Kitzmann et al. 2013). In other cases, the cloud development seems to be too infrequent, or the cloud layer is optically too thick. The estimates above may seem to be against the relevance of scattering greenhouse effect to the realization of possibly warm early Martian climate, since the only favorable case obtained is the experiment that does not permit supersaturation. However, one should be cautious about the direct applicability of the results obtained under the idealized setup of the present study to the real Martian climate problem.

In this study, we begin with a simpler problem. We have assumed temporally and spatially homogeneous values of number mixing ratio of condensed particles. However, it can vary owing to the supply of condensation nuclei by dust lifting and the removal by gravitational sedimentation. If this process is included, the variability of cloud amount obtained in Colaprete and Toon (2003) mentioned earlier will possibly be incorporated in addition to the intermittency in the present calculation resulting from energy cycle. We have to note that the number, or population, of condensed particles is quite different from that of aerosols and is known to depend on the cooling rate of air parcel (Colaprete and Toon 2003). Further, processes of collision, aggregation, and breakup of cloud particles, which should modify the particle size distribution after condensation, remain to be considered. As liquid particles were presumably absent in early Martian CO_2 atmosphere whose temperature is well above the triple point of CO_2, the efficiency of aggregation would be lower than in Earth's lower troposphere. Still it can have nonnegligible effect, considering that small but nonzero aggregation efficiency is obtained for the ice particles in Earth's cirrus clouds (Kajikawa and Heymsfield 1989). To evaluate the effects of these detailed microphysical processes, in addition to calculation of spatial and temporal variation of number mixing ratio of condensation nuclei, more sophisticated scheme of cloud microphysics is required. These issues remain to be addressed in future researches.

Also for the simplicity, we have not solved the radiative transfer process explicitly, but have introduced constant body cooling instead. However, previous studies based on one-dimensional radiative–convective equilibrium models show that extinction by CO_2 gas contributes to cooling of condensation layer, and extinction by CO_2 ice clouds contributes to both cooling and heating (Forget and Pierrehumbert 1997; Mitsuda 2007). It is not trivial to anticipate how the results of the present experiment are modified when the idealistic body cooling is replaced by a sophisticated radiative process. It could be computationally demanding task, considering the recent research of Kitzmann et al. (2013), where a discrete ordinate method with 24 streams is employed to demonstrate that conventional two-stream approximation significantly overestimates scattering greenhouse effects. Experiments including absorption and scattering of radiation by CO_2 gas and CO_2 ice cloud, as well as diurnal variation of insolation and ground temperature, are left for future work.

Acknowledgments. The reviewers, Raymond T. Pierrehumbert and two anonymous individuals, and the editor Olivier Pauluis are deeply acknowledged for reading the manuscript very carefully and providing many critical and helpful comments. This study was supported by JSPS KAKENHI Grant JP15740283, JP22740304, and MEXT KAKENHI Grant JP23103003. Numerical computations were carried out mainly on the HITACHI SR16000 at Research Institute for Information Technology, Kyushu University. The NEC SX series at the Center for Global Environmental Research of National Institute for Environmental Studies, Japan, and

the Supercomputer System at Japan Aerospace Exploration Agency are used for preliminary calculations. Products of GFD Dennou Club (http://www.gfd-dennou.org/) including Dennou Club Library (DCL), Dennou Ruby Project tools, and gtool5 library were used.

REFERENCES

Arakawa, A., and V. R. Lamb, 1977: Computational design of the basic dynamical processes of the UCLA general circulation model. *Methods in Computational Physics*, J. Chang, Ed., Vol. 17, Academic Press, 173–265, doi:10.1016/B978-0-12-460817-7.50009-4.

Asselin, R., 1972: Frequency filter for time integrations. *Mon. Wea. Rev.*, **100**, 487–490, doi:10.1175/1520-0493(1972)100<0487:FFFTI>2.3.CO;2.

Betts, A., 1975: Parametric interpretation of trade-wind cumulus budget studies. *J. Atmos. Sci.*, **32**, 1934–1945, doi:10.1175/1520-0469(1975)032<1934:PIOTWC>2.0.CO;2.

Chapman, S., and T. G. Cowling, 1970: *The Mathematical Theory of Non-Uniform Gases*. Cambridge University Press, 423 pp.

Colaprete, A., and O. B. Toon, 2003: Carbon dioxide clouds in an early dense Martian atmosphere. *J. Geophys. Res.*, **108**, 5025, doi:10.1029/2002JE001967.

——, R. M. Haberle, and O. B. Toon, 2003: Formation of convective carbon dioxide clouds near the south pole of Mars. *J. Geophys. Res.*, **108**, 5081, doi:10.1029/2003JE002053.

——, J. R. Barnes, R. M. Haberle, and F. Montmessin, 2008: CO_2 clouds, CAPE and convection on Mars: Observations and general circulation modeling. *Planet. Space Sci.*, **56**, 150–180, doi:10.1016/j.pss.2007.08.010.

DeMott, P. J., D. J. Cziczo, A. J. Prenni, D. M. Murphy, S. M. Kreidenweis, D. S. Thomson, R. Borys, and D. C. Rogers, 2003: Measurements of the concentration and composition of nuclei for cirrus formation. *Proc. Natl. Acad. Sci. USA*, **100**, 14 655–14 660, doi:10.1073/pnas.2532677100.

Forget, F., and R. T. Pierrehumbert, 1997: Warming early Mars with carbon dioxide clouds that scatter infrared radiation. *Science*, **278**, 1273–1276, doi:10.1126/science.278.5341.1273.

——, R. Wordsworth, E. Millour, J.-B. Medeleine, L. Kerber, E. Marcq, and R. M. Haberle, 2013: 3D modelling of the early Martian climate under a denser CO_2 atmosphere: Temperatures and CO_2 ice clouds. *Icarus*, **222**, 81–99, doi:10.1016/j.icarus.2012.10.019.

Glandorf, D. L., A. Colaprete, M. A. Tolbert, and O. B. Toon, 2002: CO_2 snow on Mars and early Earth: Experimental constraints. *Icarus*, **160**, 66–72, doi:10.1006/icar.2002.6953.

Golden, T. C., and S. Sircar, 1994: Gas adsorption on silicate. *J. Colloid Interface Sci.*, **162**, 182–188, doi:10.1006/jcis.1994.1023.

Held, I. M., R. S. Hemler, and V. Ramaswamy, 1993: Radiative-convective equilibrium with explicit two-dimensional moist convection. *J. Atmos. Sci.*, **50**, 3909–3927, doi:10.1175/1520-0469(1993)050<3909:RCEWET>2.0.CO;2.

Hudson, J. G., and S. S. Yum, 2002: Cloud condensation nuclei spectra and polluted and clean clouds over the Indian Ocean. *J. Geophys. Res.*, **107**, 8022, doi:10.1029/2001JD000829.

Kajikawa, M., and A. J. Heymsfield, 1989: Aggregation of ice crystals in cirrus. *J. Atmos. Sci.*, **46**, 3108–3121, doi:10.1175/1520-0469(1989)046<3108:AOICIC>2.0.CO;2.

Kasting, J. F., 1991: CO_2 condensation and the climate of early Mars. *Icarus*, **94**, 1–13, doi:10.1016/0019-1035(91)90137-I.

Kaye, G. W. C., and T. H. Laby, 1995: *Tables and Physical and Chemical Constants*. 16th ed. Longman, 624 pp.

Kitzmann, D., A. Patzer, and H. Rauer, 2013: Clouds in the atmospheres of extrasolar planets—IV. On the scattering greenhouse effect of CO_2 ice particles: Numerical radiative transfer studies. *Astron. Astrophys.*, **557**, A6, doi:10.1051/0004-6361/201220025.

Klemp, J. B., and R. B. Wilhelmson, 1978: The simulation of three-dimensional convective storm dynamics. *J. Atmos. Sci.*, **35**, 1070–1096, doi:10.1175/1520-0469(1978)035<1070:TSOTDC>2.0.CO;2.

Lorenz, E. N., 1960: Energy and numerical weather prediction. *Tellus*, **12**, 364–373, doi:10.1111/j.2153-3490.1960.tb01323.x.

Louis, J., 1979: A parametric model of vertical eddy fluxes in the atmosphere. *Bound.-Layer Meteor.*, **17**, 187–202, doi:10.1007/BF00117978.

Mischna, M. A., J. F. Kasting, A. Pavlov, and R. Freedman, 2000: Influence of carbon dioxide clouds on early Martian climate. *Icarus*, **145**, 546–564, doi:10.1006/icar.2000.6380.

Mitsuda, C., 2007: Scattering greenhouse effect of radiatively controlled CO_2 ice cloud layer in a Martian paleoatmosphere (in Japanese). Ph.D. thesis, Hokkaido University, 115 pp.

Petty, G. W., 2006: *A First Course in Atmospheric Radiation*. 2nd ed. Sundog Publishing, 472 pp.

Rossow, W. B., 1978: Cloud microphysics: Analysis of the clouds of Earth, Venus, Mars, and Jupiter. *Icarus*, **36**, 1–50, doi:10.1016/0019-1035(78)90072-6.

Sabato, J. S., 2008: CO_2 condensation in baroclinic eddies on early Mars. *J. Atmos. Sci.*, **65**, 1378–1395, doi:10.1175/2007JAS2504.1.

Sugiyama, K., M. Odaka, K. Nakajima, and Y. Y. Hayashi, 2009: Development of a cloud convection model to investigate the Jupiter's atmosphere. *J. Japan Soc. Fluid Mech.*, **28**. [Available online at http://www2.nagare.or.jp/mm/2009/sugiyama/.]

——, and Coauthors, 2011: Intermittent cumulonimbus activity breaking the three-layer cloud structure of Jupiter. *Geophys. Res. Lett.*, **38**, L13201, doi:10.1029/2011GL047878.

——, K. Nakajima, M. Odaka, K. Kuramoto, and Y. Y. Hayashi, 2014: Numerical simulations of Jupiter's moist convection layer: Structure and dynamics in statistically steady states. *Icarus*, **229**, 71–91, doi:10.1016/j.icarus.2013.10.016.

The Society of Chemical Engineers Japan, 1999: *The Handbook of Chemistry and Engineering* (in Japanese). Maruzen, 1339 pp.

Tobie, G., F. Forget, and F. Lott, 2003: Numerical simulation of winter polar wave clouds observed by Mars Global Surveyor Mars Orbiter Laser Altimeter. *Icarus*, **164**, 33–49, doi:10.1016/S0019-1035(03)00131-3.

Tompkins, A. M., 2001: Organization of tropical convection in low vertical wind shear: The role of water vapor. *J. Atmos. Sci.*, **58**, 529–545, doi:10.1175/1520-0469(2001)058<0529:OOTCIL>2.0.CO;2.

Wing, A. A., and K. A. Emanuel, 2014: Physical mechanisms controlling self-aggregation of convection in idealized numerical modeling simulations. *J. Adv. Model. Earth Syst.*, **6**, 59–74, doi:10.1002/2013MS000269.